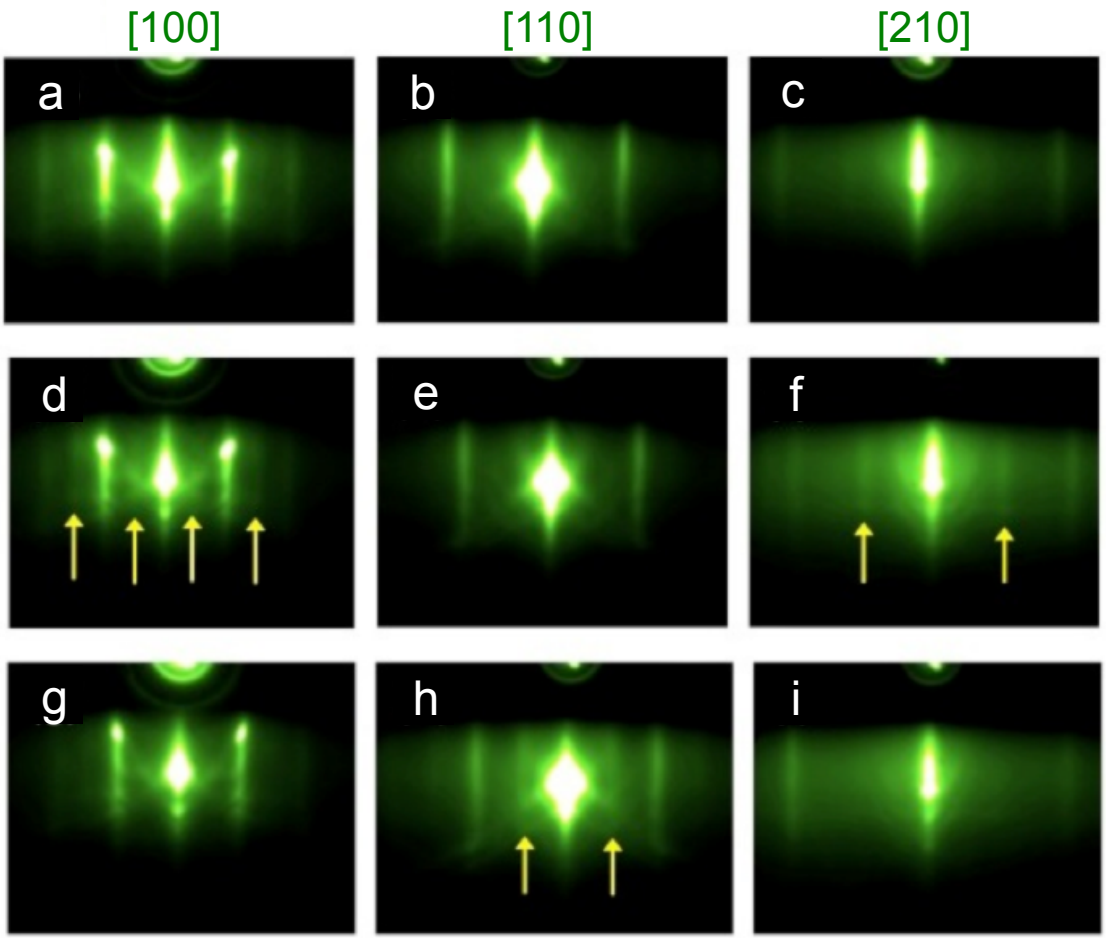

Supplementary Figure S1. Sensitivity of surface reconstruction to $La_{(1-\delta)}Al_{(1+\delta)}O_3$ stoichiometry. a-c, RHEED images taken of the neutral surface of a homoepitaxial $LaAlO_3$ film. No half-order streaks were seen along [100], [110] and [210] azimuths. **d-f,** RHEED images taken after opening the aluminum shutter for 4 s. This made the surface aluminum rich. Half-order maxima were seen along [100] and [210] azimuths as indicated by the arrows. **g-i,** RHEED images taken after making the surface slightly lanthanum rich. The arrows indicate half-order streaks seen along the [110] azimuth due to a slight excess of lanthanum.

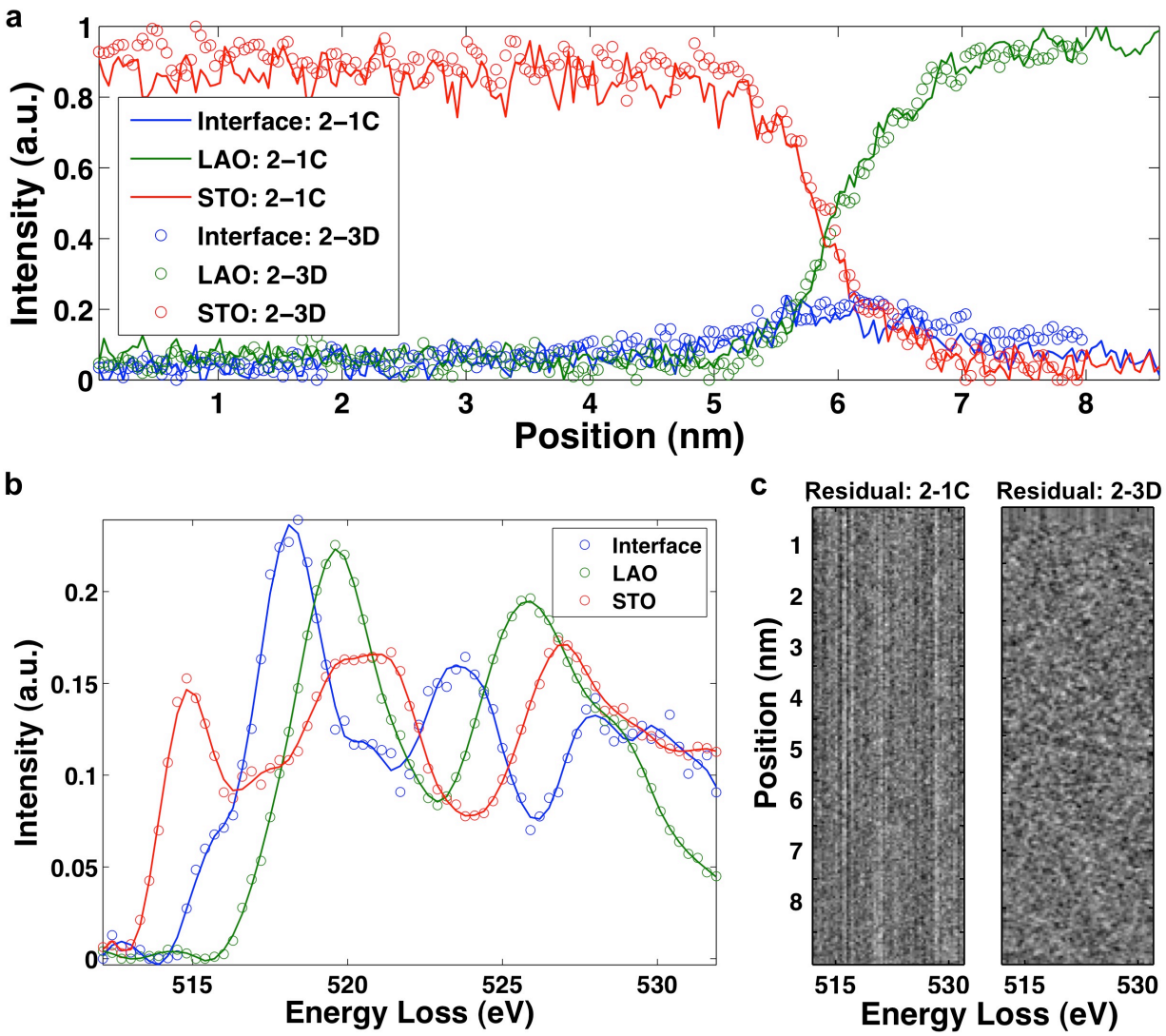

Supplementary Figure S2. EELS fine structure of the O-*K* edge of the $LaAlO_3/SrTiO_3$ interface for a conducting (2–3D) and an insulating (2–1C) sample. **a,** The concentration profile of the data fit to a $LaAlO_3$ and $SrTiO_3$ reference spectra as well as a distinct interface component extracted from the data by multivariate statistical analysis. **b**. Spectra used in the fit. Both samples show the presence of an interfacial O-*K* edge component, distinct from $LaAlO_3$ and $SrTiO_3$. This component appears, however, for both samples with the same concentration and spatial extent. **c,** The residual from the fit showing the absence of any remaining structure. The streaks for 2–1C result from a slightly different fixed pattern noise in the spectra due to a different acquisition time.

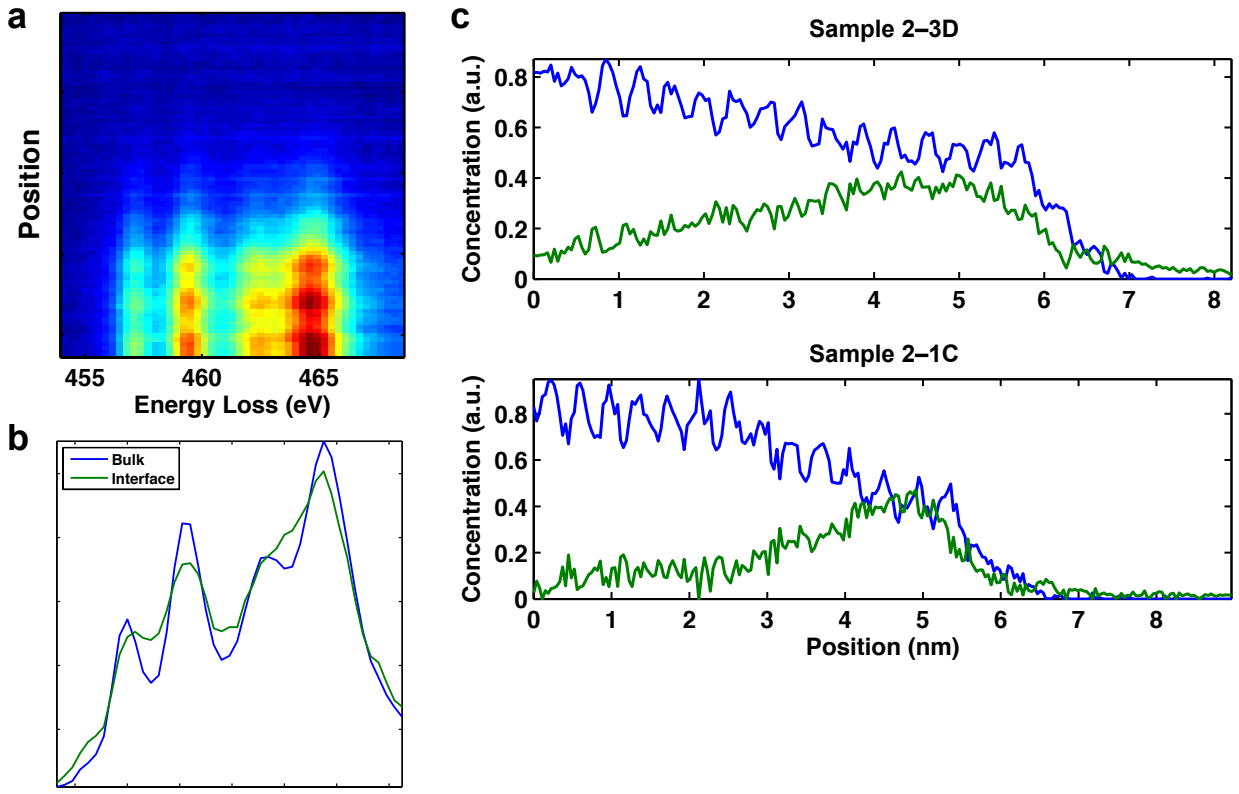

Supplementary Figure S3. STEM-EELS fine structure of the Ti-$L_{2,3}$ edge of the $LaAlO_3/SrTiO_3$ interface for a conducting (2–3D) and an insulating (2–1C) sample. a, A two-dimensional profile of the Ti-$L_{2,3}$ edge across the $LaAlO_3/SrTiO_3$ interface for the conducting interface 2–3D. The interface is interdiffused, although no shift to lower onset energy, indicative of a reduction in the titanium valence, is observed. **b**, Spectra extracted from the multivariate curve resolution analysis of the Ti-$L_{2,3}$ edge. The "interface" component tracks a reduction in the crystal field splitting from the titanium edge, possibly caused by local lattice distortions near the interface to $SrTiO_3$. The Ti-$L_{2,3}$ edge spectrum at the interface shows a significant component that is different from the bulk. A large portion is from crystal field distortions, but we cannot exclude the possibility of a small (<0.1 eV) contribution from Ti^{+3}. The spectra and the lack of a dominant Ti^{+3} component look similar to those reported for other high oxygen pressure growths of $LaAlO_3/SrTiO_3$[41,42]. **c,** Result of the fit of the spectra in (b) to the full data sets. Deviations in the quantity of the "interface" component observed could be due to slight differences in lanthanum interdiffusion for the two samples.

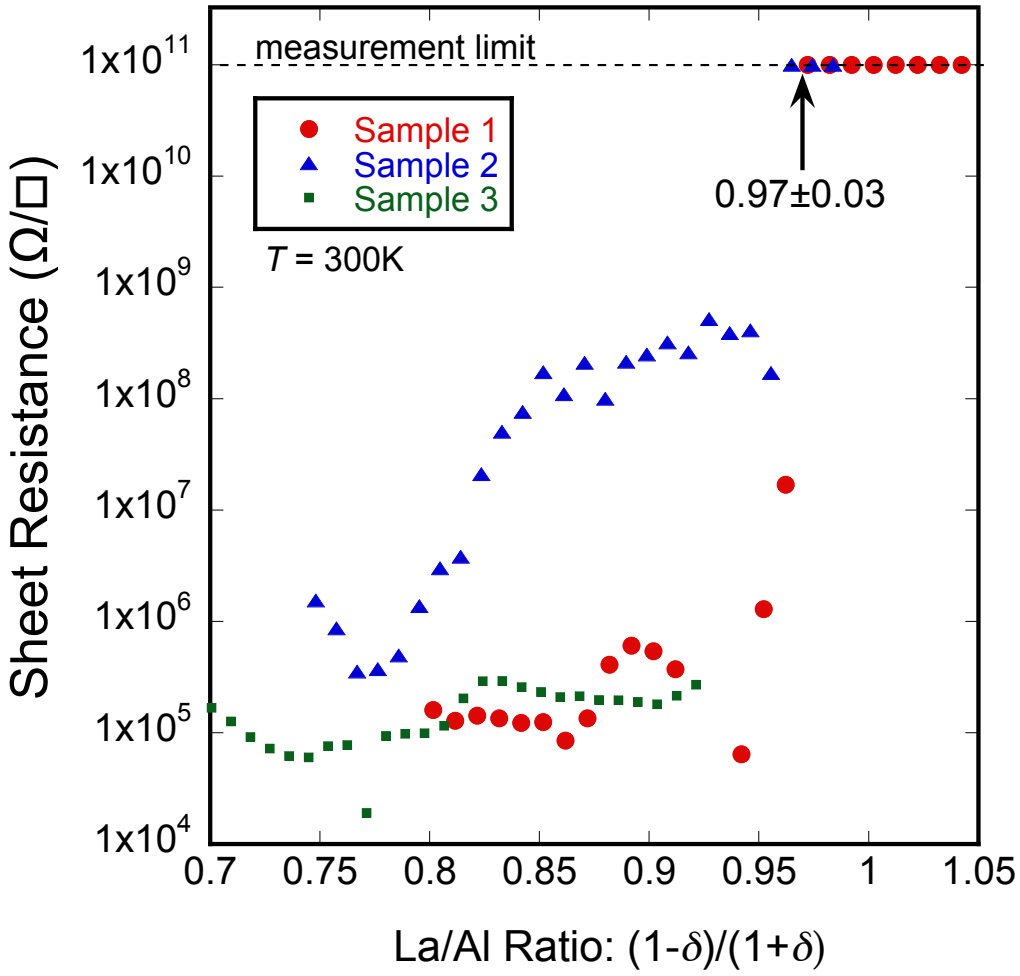

Supplementary Figure S4. Room temperature sheet resistance of $La_{(1-\delta)}Al_{(1+\delta)}O_3$ / (001) $SrTiO_3$ interfaces as a function of La/Al ratio. The data shown in Fig. 3c is plotted here on a logarithmic resistance scale. The La/Al ratio was determined by RBS measurements. Local 4-point resistance measurements were made on all devices placed at 1 mm intervals on three long samples. A sharp jump in sheet resistance is observed at a La/Al ratio of 0.97±0.03, consistent in all three samples. See the section on "Cation stoichiometry from RBS measurements" in the main manuscript for error analysis. The overall higher interface resistance observed in sample 2 is likely due to slight variations in substrate/substrate surface termination. Also, on two consecutive devices of sample 1, accurate measurements were not possible presumably due to sample processing issues. These two data points have been removed from the plot.

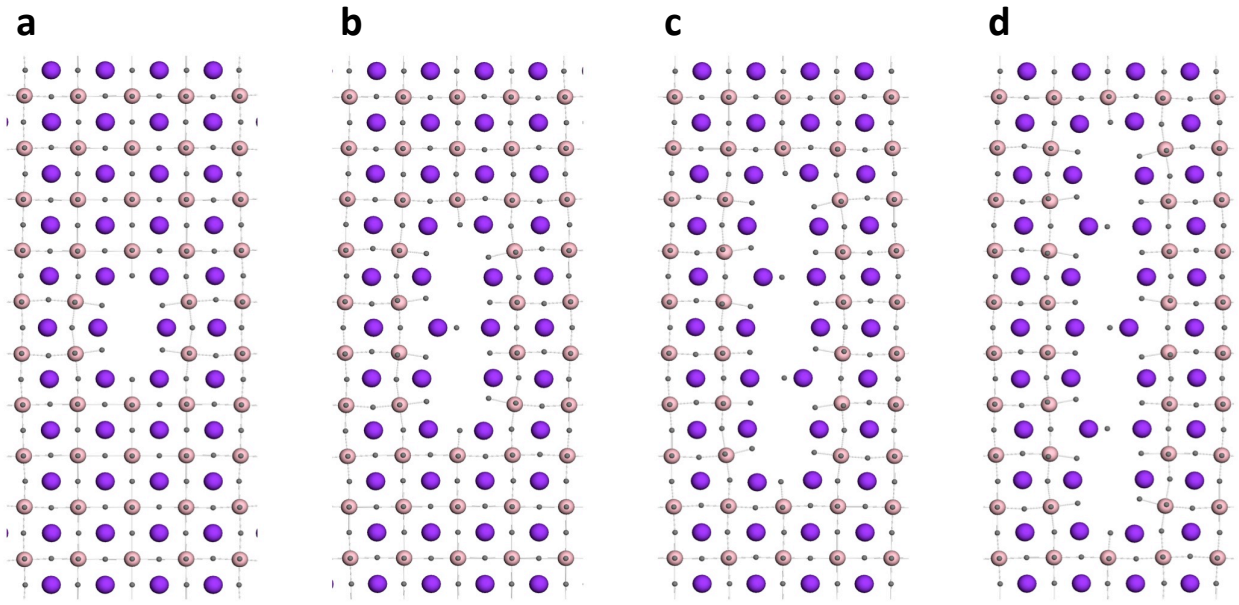

Supplementary Figure S5. Al_2O_3 vacancy complexes. The lowest energy Al_2O_3-vacancy-complexes with widths n = 2, 4, 6, and 8 are shown from above. **a,** n = 2. **b,** n = 4. **c,** n = 6. **d,** n = 8. For $n \geq 4$, there are oxygen ions in the vacancy columns. Both the oxygen ions and the nearest lanthanum ions are shifted by half a lattice constant in the z direction (into the page). The stoichiometry is held fixed at approximately $(1-\delta)/(1+\delta)$ = 16/15 by increasing the supercell size with increasing n.

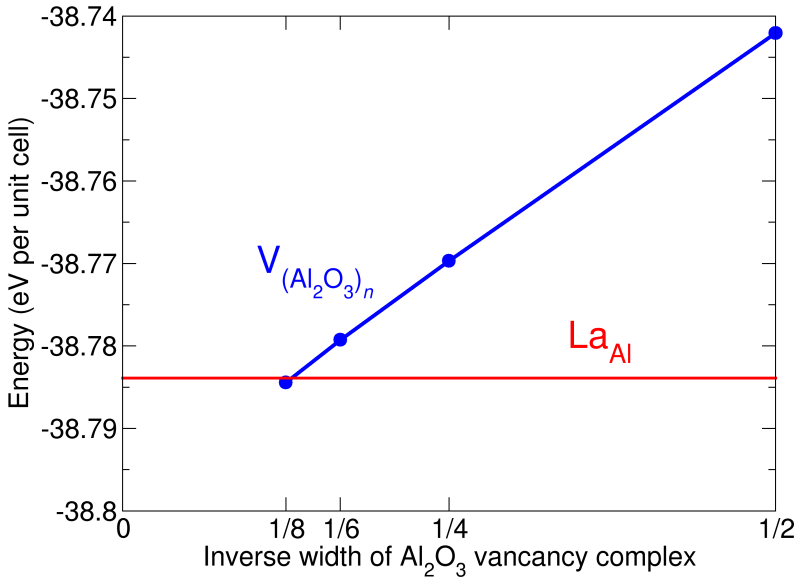

Supplementary Figure S6. Energy of the Al_2O_3-vacancy-complexes as a function of inverse width *n*. The energy of the La_{Al} substitutional defect (see Supplementary Fig. S7) is shown in red.

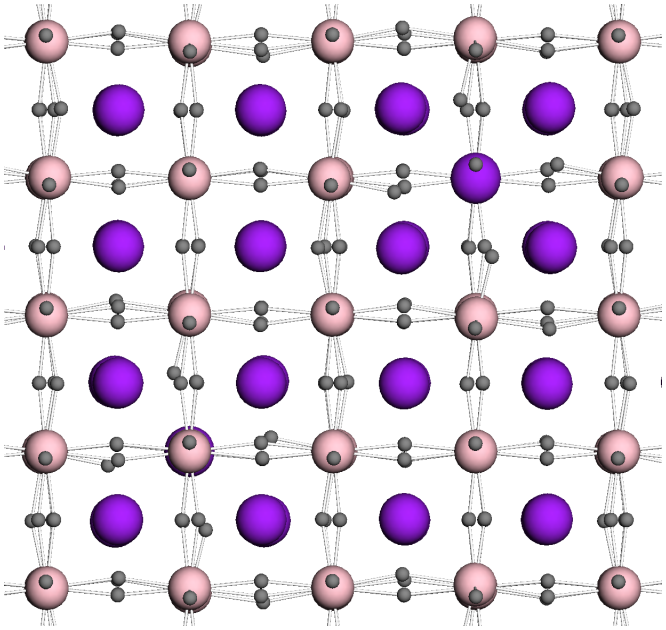

Supplementary Figure S7. La_{Al} substitutional defect. Structure of the $La_{33}Al_{31}O_{96}$ calculation with La_{Al} substitutional defects viewed from the side. The stoichiometry is $(1-\delta)/(1+\delta) = 33/31$.

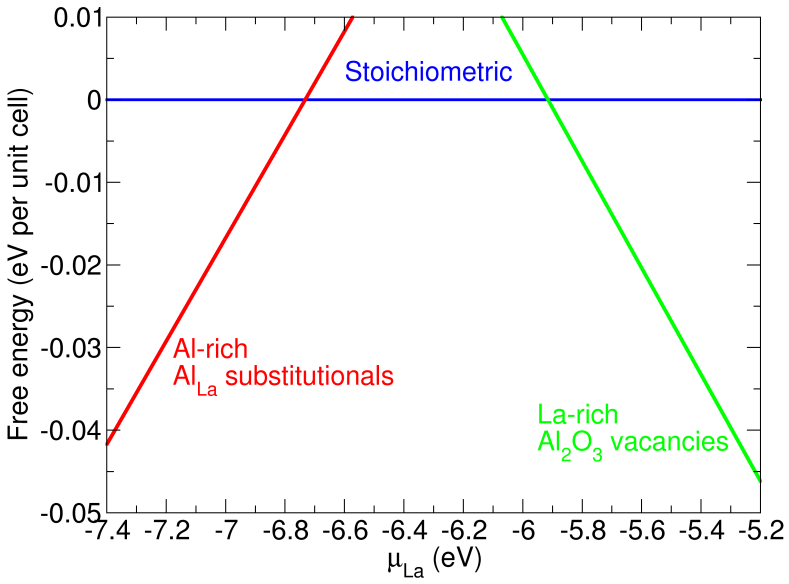

Supplementary Figure S8. Free energies of bulk $La_{(1-\delta)}Al_{(1+\delta)}O_3$ strained to the $SrTiO_3$ lattice constant at various stoichiometries. The three lines show the free energy of ideal stoichiometric $LaAlO_3$ (blue) and the lowest energy aluminum-rich (red) and lanthanum-rich (green) structures. The stoichiometric energy is taken as the reference. The aluminum-rich compound is $La_{31}Al_{33}O_{96}$, with aluminum substituting for lanthanum as in Fig. 5a. The lanthanum-rich compound is $La_{128}Al_{120}O_{372}$, with the $(Al_2O_3)_8$-vacancy-complex in Supplementary Fig. S5d. This plot is used to set the range of μ_{La} for which each stoichiometry is stable.

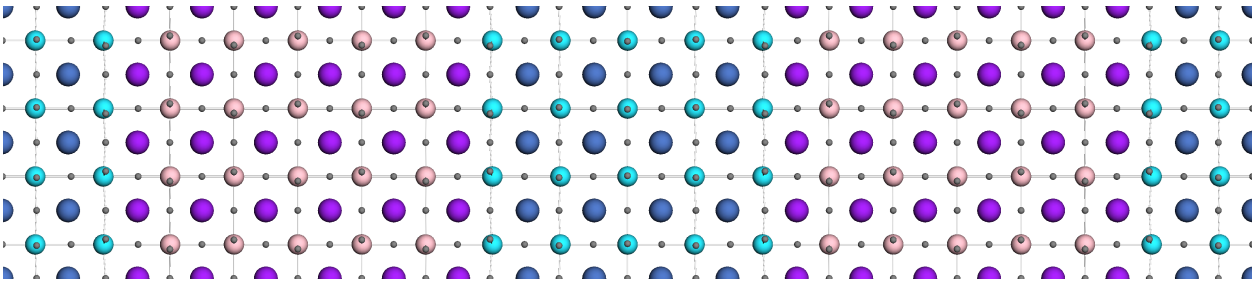

Supplementary Figure S9. Structure used for the interface computations. A multilayer geometry consisting of 5.5 unit cells of $LaAlO_3$ (pink and purple) and 4.5 unit cells of $SrTiO_3$ (light and dark blue) was used. There are two identical defect-free LaO/TiO_2 interfaces, resulting in 1/2 electron per interface per areal cell in the conduction band.

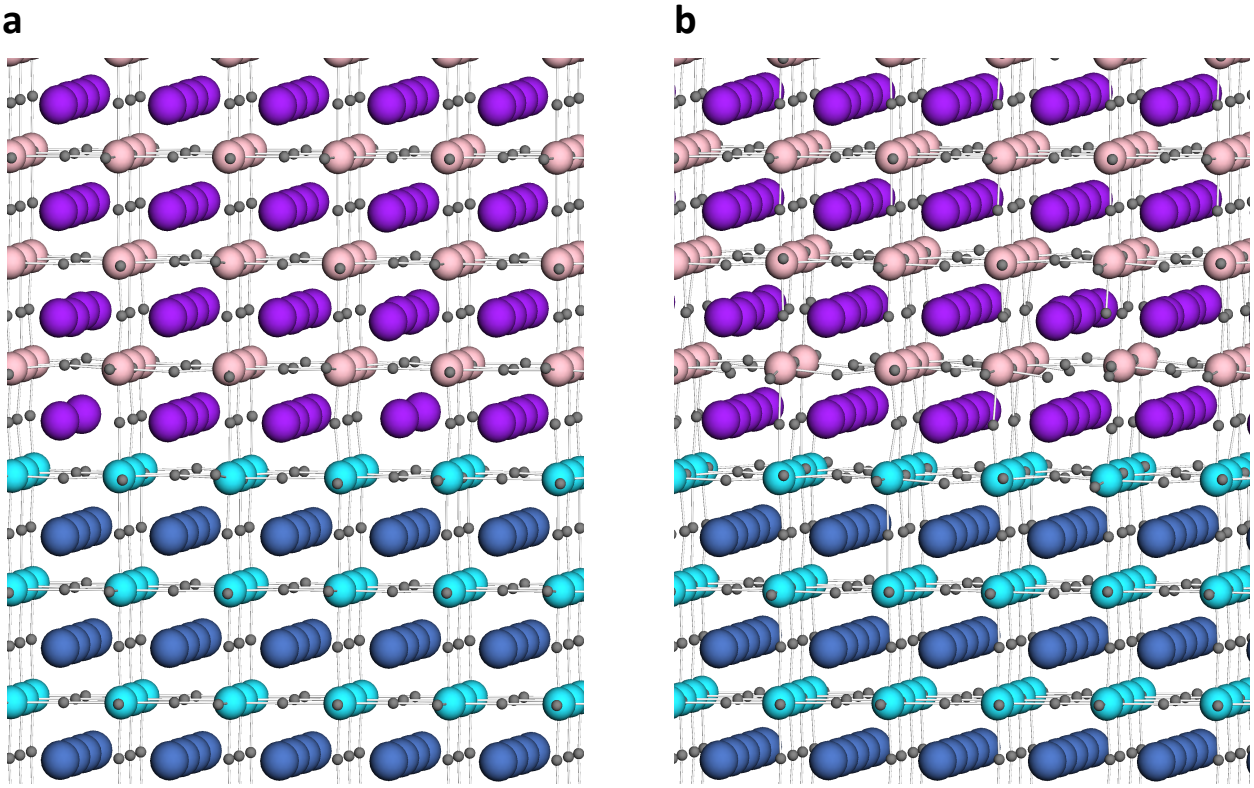

Supplementary Figure S10. The structures with cation vacancies at the interface. a, La vacancies. **b**, Al vacancies. The vacancy densities are 1/6 monolayers. Both defects have charge +3, and the structures are insulating.

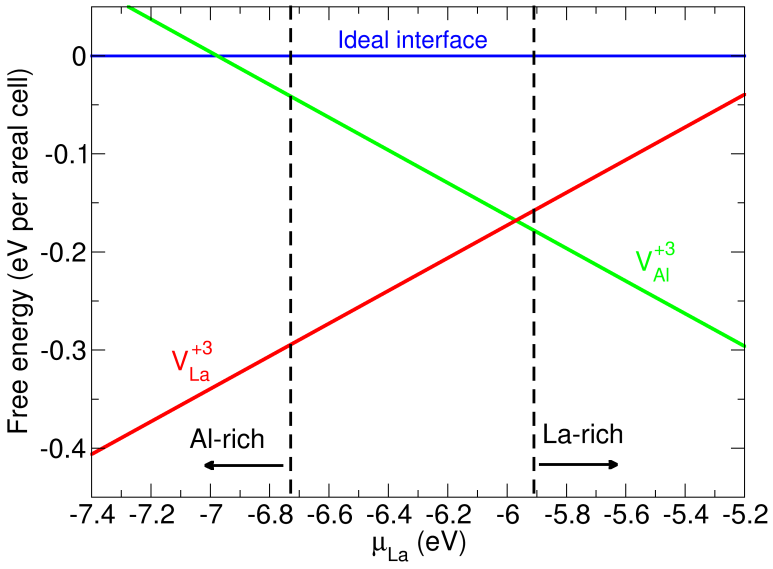

Supplementary Figure S11. Free energies of the $La_{(1-\delta)}Al_{(1+\delta)}O_3/SrTiO_3$ interface structures. The ideal defect-free $LaAlO_3/SrTiO_3$ interface (blue line and Supplementary Fig. S9) has a 2-DEL at the interface. Lanthanum vacancies with charge +3 (red line and Supplementary Fig. S10a) at the interface are stable for lower μ_{La}, and aluminum vacancies also charged +3 (green line and Supplementary Fig. S10b) are stable for higher μ_{La}. The dashed lines show the ranges of μ_{La} for each stoichiometry determined in Supplementary Fig. S8. As described in the text, the aluminum-rich films prevent cation migration, and vacancies cannot form at the interface.

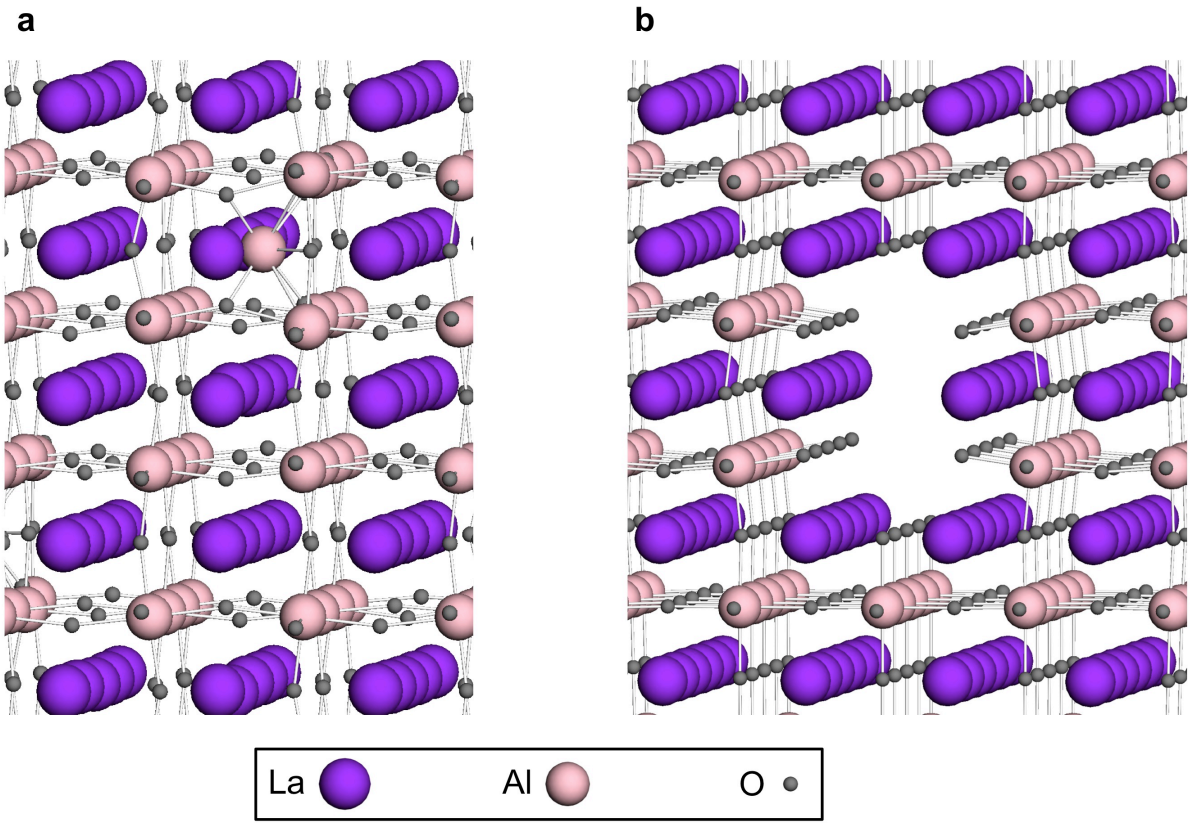

Supplementary Figure S12. Different views of lowest energy structures determined with density functional theory. a, In Al-rich films, Al substitutes for La and shifts off center. The lowest-energy structure is shown as viewed slightly tilted from the [100] direction. **b,** In La-rich films, Al_2O_3-vacancy-complexes form, which are periodic in the [001] direction. The smallest Al_2O_3-vacancy-complex is shown as viewed slightly tilted from the [001] direction.

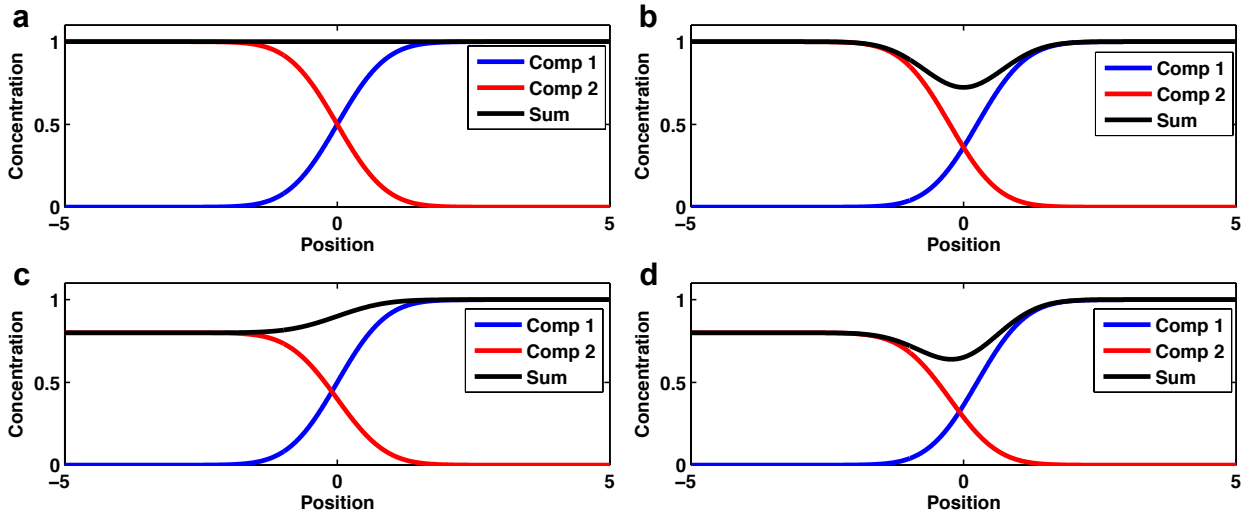

Supplementary Figure S13. Simulation to confirm normalization of cation concentration. a, A simulation of a vacancy free interface with interdiffusion (error function line shape). The total sum of the two components is unity throughout the interface. **b,** Simulation of two normalized components, however with a 25% reduction in the total atomic concentration at the interface. A clear dip in the total concentration is observed, similar to Fig. 6d. **c,** Simulation of two components, one of which has 80% occupancy but free of additional vacancies at the interface. There is no local dip in the total concentration at the interface below the mean values on either side. **d,** Simulation of two components, one of which has 80% occupancy and additional vacancies added at the interface. Once again a local drop in the total atomic profile is seen at the interface.

Supplementary Table S1. Resistance, capacitance and loss tangent measurements on $SrTiO_3$ substrates exposed to different conditions.

Substrate piece	Measurements at 295 K			Measurements at 77 K	
	Resistance	Capacitance (pF)	Loss tangent	Capacitance (pF)	Loss tangent
p (vacuum)	< 20 KΩ	-	-	-	-
q (O_2)	> 10 GΩ	46.1	0.0013	241.2	0.0007
r (O_3)	> 10 GΩ	57.8	0.0005	334.3	0.0002
s (control)	> 10 GΩ	46.3	0.0002	268.2	0.0003

Supplementary Note 1.
Lanthanum and aluminum flux calibration by homoepitaxial growth

The precise calibration of lanthanum and aluminum fluxes prior to the growth of $La_{(1-\delta)}Al_{(1+\delta)}O_3$ on (001) $SrTiO_3$ substrates is critical to the results discussed in this study. To achieve this calibration, the temperatures of both the lanthanum and the aluminum sources were first adjusted to obtain a flux of approximately 1.3×10^{13} atoms/(cm^2·s) for each element. The approximate fluxes were measured with a quartz crystal microbalance (QCM) using tooling factors predetermined for each source by *ex situ* Rutherford back scattering measurements. With the lanthanum and aluminum fluxes approximately matched, homoepitaxial $LaAlO_3$ was grown on (001) $LaAlO_3$ substrates via codeposition (both lanthanum and aluminum shutters were simultaneously opened and left open) in a distilled ozone background partial pressure of 1×10^{-6} Torr and a substrate temperature of ~680 ºC. The strategy here was to exactly match the lanthanum and aluminum fluxes by carefully adjusting the aluminum source temperature using *in situ* reflection high-energy electron diffraction (RHEED) feedback obtained during this homoepitaxial $LaAlO_3$ growth. This process is discussed below.

The calibration sample was continuously rotated during growth. This allowed for simultaneous monitoring of the RHEED patterns of the growing surface layer along multiple in-plane crystallographic directions. Weak, but distinct signatures in the RHEED patterns were empirically determined that corresponded to slight excesses of lanthanum or aluminum in the surface layer. Supplementary Fig. S1 shows a representative set of RHEED images obtained at the end of a homoepitaxial calibration growth once the lanthanum and aluminum fluxes were perfectly matched. The distilled ozone partial pressure was maintained at 1×10^{-6} Torr as these images were acquired. The top row of images, Fig. S1a to Fig. S1c, show RHEED patterns obtained along the [100], [110] and [210] azimuths, respectively, from the neutral surface with no excess of either lanthanum or aluminum atoms. Sharp RHEED patterns are observed along all three directions just like that of a $LaAlO_3$ substrate with no extra streaks characteristic of surface reconstructions. Subsequently, the center row of images, Fig. S1d to Fig. S1f, were obtained after depositing ~7% excess of aluminum achieved by opening only the aluminum shutter for just 4 seconds (~55 seconds corresponds to a monolayer of aluminum). Weak half-order streaks can be observed along both the [100] azimuth (Fig. S1d) and the [210] azimuth (Fig. S1f) and are indicated by yellow arrows. Finally, the bottom row of images, Fig. S1g to Fig. S1i, were captured from a surface with ~7% excess of lanthanum achieved by depositing only lanthanum for ~8 seconds. Note that the first 4 seconds of lanthanum balanced the excess aluminum on the surface leading to neutral RHEED patterns (as shown in Fig. S1a to Fig. S1c) while the last 4 seconds led to ~7% excess of lanthanum. The lanthanum rich surface is characterized by half order streaks only along the [110] azimuth indicated by yellow arrows (Fig. S1h). Note that if the surface becomes much more lanthanum rich, faint half-order streaks could appear along the [210] azimuth as well (not shown), but not along the [100] azimuth.

The half-order streaks that appear in the RHEED patterns during growth of the homoepitaxial $LaAlO_3$ calibration film along the different in-plane directions provided sensitive feedback enabling the lanthanum and aluminum fluxes to be matched. If the RHEED patterns began to show signatures of an aluminum (lanthanum) rich surface, as lanthanum and aluminum are codeposited starting from a neutral surface, first, the aluminum (lanthanum) shutter was closed for a few seconds at a time to reduce the aluminum (lanthanum) content of the surface layer until the surface was reversed. i.e., RHEED showed signatures of a surface rich in the other species.

At this point the aluminum source temperature was lowered (increased) on the fly by as small a step as 0.1 ºC, which corresponds to a change in aluminum flux as low as ~0.2%. With this change in aluminum flux, the RHEED patterns were closely monitored. If after some time of codeposition, the RHEED patterns still developed characteristic features corresponding to the excess of one species, the above steps were repeated to reduce the difference in the flux between lanthanum and aluminum. This process was carried out until the $LaAlO_3$ calibration sample could be grown via codeposition for over 20 minutes (~20 unit cells thick) with the RHEED indicating a neutral surface layer without having to close the shutters or make any temperature adjustments to the sources. Based on the assumption that an excess of a species accumulates mostly at the surface, at this point the lanthanum and aluminum fluxes are matched to better than 0.4% since this would result in over a 7% excess at the surface during the 20 layers of growth and would be easily observed in RHEED as shown in Supplementary Fig. S1. With the lanthanum and aluminum fluxes matched to better than 0.4%, the calibration growth was terminated and the (001) $SrTiO_3$ substrate was loaded into the chamber and the growth of the actual sample immediately followed.

Supplementary Note 2

Following the report of our results[43], which revealed the important role of $LaAlO_3$ cation stoichiometry for the formation of the 2-DEL, other groups have carried out related experiments[35,44-50]. The systems studied include non-conducting interfaces found in sputtered $LaAlO_3$ on (001) $SrTiO_3$, where the $LaAlO_3$ films are La-rich[35,44]; non-conducting interfaces in samples grown by PLD at high oxygen pressure that are found to contain up to 20% more lanthanum than films grown at lower pressures, which exhibit conductive interfaces[45]; and samples grown by PLD for which the stoichiometry of the $LaAlO_3$ films are found to be modified from sample to sample by adjusting the conditions of the laser plume[46-48]. The results of these investigations are consistent with our findings. They provide further evidence for the existence of a critical La/Al ratio (determined to be 0.97 ± 0.03 in our MBE-grown films) being necessary for interface conductivity when extrinsic defects, intermixing[49], and oxygen vacancies[50] are minimized.

Supplementary Note 3.
First principles predictions of defect structure and electronic properties of off-stoichiometric $La_{(1-\delta)}Al_{(1+\delta)}O_3$ films

The density functional calculations used the generalized-gradient approximation[51] and projector-augmented wave functions[52] as implemented in VASP[53,54]. A 282.8 eV planewave cutoff was used for the basis set. In all calculations, the in-plane lattice constant was fixed to the theoretical $SrTiO_3$ lattice constant, a_{SrTiO_3} = 3.948 Å.

The section can be outlined as follows: (1) Defects form when $LaAlO_3$ is grown off stoichiometry. (2) The extended Al-O vacancy complexes formed in lanthanum-rich films allow ionic motion between the interface and surface while the localized aluminum-rich defects do not. (3) In the limit of thick $LaAlO_3$ films, cation vacancies will form spontaneously at the interface to compensate the diverging potential[14] if given the chance, but this mechanism is negligible in thin films. (4) In lanthanum-rich films, the extended defects in the films allow cation vacancies

to move to the interface to compensate the diverging potential in thicker films. The localized defects in the aluminum-rich films allow negligible cation motion, and a metallic interface forms after the film reaches a critical thickness.

First we determine which defects form in bulk $La_{(1-\delta)}Al_{(1+\delta)}O_3$ strained to the $SrTiO_3$ lattice constant. La/Al stoichiometries of approximately $(1-\delta)/(1+\delta)$ = 15/16 and 16/15 (0.9375 and 1.0667) were used. For the aluminum-rich calculations, the Al_{La} substitutional defect shown in the main paper had an energy more than 60 meV per unit cell lower than the lowest energy La-O vacancy complex that we found[55].

In the lanthanum-rich case, the lowest energy Al-O vacancy complexes are columns of $(Al_2O_3)_n$ vacancies, shown in Supplementary Fig. S5. As the width n of the vacancy columns increases, the energy decreases roughly linearly with $1/n$ as seen in Supplementary Fig. S6. For $n \geq 8$, the energy of the $(Al_2O_3)_n$ vacancy column is less than the energy of the La_{Al} substitutional defect, shown in Supplementary Fig. S7. Even for $n < 8$, once an $(Al_2O_3)_n$ vacancy forms in one layer, it is likely to persist in subsequently grown layers.

To compare structures with different stoichiometries energetically, we compute the Gibbs free energy,

$$G = E - \mu_{La}N_{La} - \mu_{Al}N_{Al} - \mu_{O}N_{O}, \quad (1)$$

where E is the total energy of the system computed with DFT, the N_i are the numbers of each atom in the calculation, and the μ_i are the chemical potentials. The potentials are subject to the constraint

$$\mu_{La} + \mu_{Al} + 3\mu_{O} = \mu_{LaAlO_3}^{bulk}, \quad (2)$$

where $\mu_{LaAlO_3}^{bulk}$ is the computed energy of bulk $LaAlO_3$ strained in the x-y plane to the $SrTiO_3$ lattice constant and relaxed in the z direction. The growth conditions (680 ºC and 10^{-6} Torr of distilled ozone) determine μ_O[56]. Thus there is only one independent parameter: We will vary μ_{La} and determine μ_{Al} from Eq. (2).

The energies of the stoichiometric, aluminum-rich, and lanthanum-rich phases of bulk $La_{(1-\delta)}Al_{(1+\delta)}O_3$ strained to the $SrTiO_3$ lattice constant are plotted in Supplementary Fig. S8. We use this plot to determine the ranges of μ_{La} over which each phase is stable. For $\mu_{La} < -6.73$ eV, the film is aluminum-rich, while for $\mu_{La} > -5.91$ eV, it is lanthanum-rich.

Structures with higher energies are not shown. There has been interest in the role of oxygen vacancies in this system. We find that the formation energy of oxygen vacancies in bulk $LaAlO_3$ is high and is not affected by either Al_2O_3 vacancy complexes or La_{Al} substitutional defects – The oxygen vacancy formation energies are the same as in stoichiometric $LaAlO_3$[57].

We now turn to calculations of $La_{(1-\delta)}Al_{(1+\delta)}O_3$ films on $SrTiO_3$. In the limit of thick ideal $LaAlO_3$ films on $SrTiO_3$, ½ electron is transferred to the $SrTiO_3$ conduction band, and there is no electric field in the $LaAlO_3$[14,17]. The surface reconstructs to assume a positive charge; it has been shown that oxygen vacancies form spontaneously at the surface of sufficiently thick $LaAlO_3$ on $SrTiO_3$[36]. Note that oxygen vacancies in the $SrTiO_3$ substrate, however, do not screen the field in the $LaAlO_3$ since these vacancies lie on the same side of the $LaAlO_3$ as the electrons in the $SrTiO_3$ conduction band. We approximate the limit of thick $LaAlO_3$ films using the multilayer

structure shown in Supplementary Fig. S9, with two identical interfaces and no surfaces. The $LaAlO_3$ has one more LaO layer than AlO_2 layers, resulting in 1 electron in the conduction band, which is shared by the two interfaces. Due to mirror symmetry, there is no electric field in the middle of the $LaAlO_3$.

We examine the stability of charged defects at the $La_{(1-\delta)}Al_{(1+\delta)}O_3/SrTiO_3$ interface by putting lanthanum and aluminum vacancies in the multilayer calculations, keeping the mirror symmetry. The vacancy structures are shown in Supplementary Fig. S10. At a vacancy density of 1/6 monolayers, the +3 defects remove the 1/2 electron at the interface forming an insulator. As seen in Supplementary Fig. S11, the ideal interface with the 2-DEL has higher energy than the insulating interfaces with cation vacancies under all conditions.

Interestingly, the lanthanum vacancies at the interface gain energy by diffusing into the $SrTiO_3$, forming a strontium substitutional defect and a strontium vacancy, which can diffuse far from the substitutional. Thus any *A*-site deficiency will be spread out over many layers.

In summary, we have computed the nature of the defects that form in off-stoichiometric $La_{(1-\delta)}Al_{(1+\delta)}O_3$ strained to the $SrTiO_3$ lattice constant. In aluminum-rich samples, aluminum substitutes for lanthanum. In lanthanum-rich samples, Al_2O_3-defect-complexes form. The energetics of the defects allows us to determine the ranges of chemical potentials for each stoichiometry.

Importantly, the Al_2O_3-vacancy-complexes allow ionic movement between the surface and the interface, while the Al_{La} substitutional defects do not. In calculations simulating thick $LaAlO_3$ films on $SrTiO_3$, we find cation vacancies form spontaneously to compensate the electron liquid. The scenario is outlined in Fig. 5: The $La_{(1-\delta)}Al_{(1+\delta)}O_3$ films grow with defects to accommodate the stoichiometry, and the electrostatic potential difference between the surface and interfaces grows with the film thickness[14]. In the aluminum-rich films, the diverging potential is eventually screened by the formation of an interfacial electron liquid. In the lanthanum-rich films, aluminum vacancies can easily move to the interface through the Al_2O_3-vacancy-complexes to screen the diverging potential, and the system remains insulating.

Supplementary Note 4.
Cation composition mapping using STEM-EELS

STEM-EELS spectroscopic images were acquired on samples 2–4A and 2–4B, representative La-rich and Al-rich films, grown on pieces of $SrTiO_3$ cut from the same initial substrate. The Ti-$L_{2,3}$, La-$M_{4,5}$ and Al-*K* edges were acquired simultaneously to compute the total concentration of titanium and aluminum on the *B*-site. Due to limitations in the number of channels accessible on the EELS spectrometer, this was immediately followed by an acquisition of the La-$M_{4,5}$, Al-*K* and Sr-$L_{2,3}$ edges from a neighboring region on the TEM wedge to determine the concentration of lanthanum and strontium on the *A*-site.

The concentration of the cations was determined by performing a power law background subtraction and integration over approximately 10 eV. EELS scattering cross-sections are only accurate to about 30% for comparison between different shells, and thus could not be used to normalize the signal with sufficient precision for this study. The strontium and titanium signals

were normalized from signal in the $SrTiO_3$ substrate sufficiently far from the interface. The lanthanum and aluminum signals were normalized from the signal in the $LaAlO_3$ film; all signals were normalized to "1" regardless of the composition of the film. While this normalization cannot be used to determine total concentration, it does preserve the presence or absence of local, relative variations in concentration such as the local dip in *B*-site concentration observed for sample 2–4A. As shown in Supplementary Fig. S13, if there is no concentration dip at the interface, the normalization cannot introduce one. We also tested the normalized data to the RBS concentrations from the partner set of films, and found the same trends.

Supplementary Note 5.
Oxygen vacancies in $SrTiO_3$ due to growth conditions

The orders of magnitude lower oxygen partial pressures that are generally used in oxide molecular-beam epitaxy in contrast to pulsed-laser deposition is considered to lead to oxygen vacancies, which are well known to dope $SrTiO_3$ substrates with electrons. This overwhelms phenomena occurring at the $La_{(1-\delta)}Al_{(1+\delta)}O_3/SrTiO_3$ interface if the oxygen content of the sample, including the substrate, is not carefully maintained. The samples studied in this work were grown with a distilled ozone source instead of molecular oxygen. The high oxidation power of ozone in contrast to molecular oxygen enables the growth of fully oxygenated samples at lower ozone partial pressures.

To qualitatively determine the oxygen vacancy content in $SrTiO_3$ substrates once exposed to growth conditions, electrical measurements were carried out on a $SrTiO_3$ substrate that was cut into four, 5 mm × 5 mm pieces, labeled *p*, *q*, *r* and *s*. The four $SrTiO_3$ substrate pieces were first etched and annealed via the same steps used to prepare the $SrTiO_3$ substrates for the samples studied in this work. i.e., following the standard procedure[31] to obtain a TiO_2 terminated surface. Using a shadow mask with a large via hole of ~ 4 mm × 4 mm, a 100 Å thick chrome layer followed by a 1300 Å thick gold layer were thermally evaporated (at room temperature in a vacuum of $\sim 1\times10^{-5}$ Torr) on the center of the backside of each of these substrate pieces taking care that the chrome-gold layer did not touch the substrate edges. This chrome-gold layer served two purposes: it enabled radiative heating of the substrates in vacuum and later served as a large-area-contact for electrical measurements.

A sample holder with a 4 mm × 4 mm opening was used to mount the substrate pieces such that they could be radiatively heated from the backside. Substrate pieces *p*, *q* and *r* were consecutively loaded into the MBE chamber and exposed to different conditions while the last $SrTiO_3$ piece *s*, served as a control for comparing the electrical data and remained under atmospheric conditions. Substrate piece *p* was heated inside the MBE chamber to 680 °C in a base vacuum of $\sim 6\times10^{-9}$ Torr. Substrate piece *q* was heated to the same growth temperature of 680 °C, but in a molecular oxygen background partial pressure of 1×10^{-6} Torr while substrate piece *r* was similarly heated to 680°C in the presence of ozone providing a background pressure of 1×10^{-6} Torr. In all cases the 680 ºC substrate temperature was sustained for 20 minutes (the typical growth time for the 8 unit cell thick $La_{(1-\delta)}Al_{(1+\delta)}O_3$ on $SrTiO_3$ films studied in this work) before cooling down. The substrate pieces *q* and *r* were cooled to 200 ºC while maintaining the same oxygen or ozone background pressure at which point the molecular oxygen or ozone flow was closed and the substrates were immediately taken out of the MBE chamber and exposed to

atmospheric conditions. Note that substrate piece *r* was exposed to the same conditions as the $La_{(1-\delta)}Al_{(1+\delta)}O_3/SrTiO_3$ samples studied in this work with the absence of opening and closing the source shutters to grow a $La_{(1-\delta)}Al_{(1+\delta)}O_3$ film.

At this point, using a shadow mask with a via of ~ 4 mm × 4 mm, a 100 Å thick chrome layer followed by a 1300 Å thick gold layer was thermally evaporated as before on the center of the top surface of each of these substrate pieces. The top and bottom metal contacts enabled us to make resistance measurements (perpendicular to the surface) of the $SrTiO_3$ substrate pieces as well as capacitance measurements in a parallel-plate capacitor geometry. Resistance and capacitance measurements made on these samples at room temperature (~295 K) and at 77 K are given in Supplementary Table S1.

As expected the substrate piece *p*, which was heated in vacuum was found to be quite conductive (resistance less than 20 KΩ at room temperature) due to loss of oxygen. Capacitance measurements on this substrate were therefore, not feasible. The other substrate pieces were all very insulating with resistances greater than 10 GΩ (the maximum resistance that can be measured with our Keithley nanovoltmeter/current source measurement setup). Capacitance and loss tangent measurements were made at 100 Hz and 1 KHz with an Andeen Hagerling (AH2700A) capacitance bridge on these substrate pieces. As a representative data set, measurements made at 1 KHz are shown in table S1 since both frequencies gave similar capacitance and loss tangent values. The difference in capacitance between the different substrate pieces is mainly due to the ± 15% variation in the surface area of the chrome-gold contacts that form the top and bottom electrodes. The large increase in capacitance from room temperature to 77 K (by approximately a factor of 5) is a result of the increase in the dielectric constant of $SrTiO_3$ as the temperature is lowered.

The loss tangent measurements are proportional to the leakage current that could be due to a presumable loss of oxygen in these substrate pieces. It should be noted that both room temperature and 77 K measurements were made with the substrate pieces mounted on a probe. The long and not completely balanced wires between the substrates and the capacitance bridge were found to set a lower bound for accurate loss tangent values to 0.0005. Values below this should be considered to be within the measurement error. Substrate piece *q*, which was heated in a background pressure of 1×10^{-6} Torr of oxygen was found to have a loss tangent above this measurement threshold both at room temperature and at 77 K, suggesting some possible loss of oxygen. It should be noted here that the oxygen/ozone injector in the MBE system is directed straight at the substrate and is located a distance of 64 mm from the substrate, which could lead to a much higher oxygen partial pressure at the substrate than the 1×10^{-6} Torr background pressure measured by an ion gauge. This possibly much higher partial pressure of oxygen at the substrate should be taken into account when considering the small increase in the loss tangent observed for substrate piece *q* compared to that of the control. The substrate piece *r*, however, which was heated in a background pressure of 1×10^{-6} Torr of distilled ozone had loss tangent values comparable to the control and below the measurement threshold. Again note that the placement of the oxygen/ozone injector in the MBE system would have provided a much higher ozone partial pressure at the substrate than the 1×10^{-6} Torr background pressure measured by an ion gauge. This data clearly demonstrates that the growth conditions used to grow the $La_{(1-\delta)}Al_{(1+\delta)}O_3/(001)$ $SrTiO_3$ films studied in this work does not lead to an extra conduction mechanism related to a loss of oxygen from the bulk of the $SrTiO_3$ substrates.

Supplementary References

41 Maurice, J. L. *et al.* Electron energy loss spectroscopy determination of Ti oxidation state at the (001) $LaAlO_3/SrTiO_3$ interface as a function of $LaAlO_3$ growth conditions. *Europhys. Lett.* **82,** 17003 (2008).

42 Verbeeck, J. *et al.* Electronic reconstruction at n-type $SrTiO_3/LaAlO_3$ interfaces. *Phys. Rev. B* **81,** 085113 (2010).

43 Warusawithana, M. P. *et al.* Effect of stoichiometry on the $LaAlO_3/SrTiO_3$ 2-D electron gas grown by MBE. *APS March Meeting 2010***,** B37.00001 (2010).

44 Dildar, I. M. *et al.* Conductivity of $LaAlO_3/SrTiO_3$ interfaces made by sputter deposition. *e-J. Surf. Sci. Nanotech.* **10,** 619-623 (2012).

45 Kalabukhov, A. *et al.* Improved cationic stoichiometry and insulating behavior at the interface of $LaAlO_3/SrTiO_3$ formed at high oxygen pressure during pulsed-laser deposition. *Europhys. Lett.* **93,** 37001 (2011).

46 Schoofs, F. *et al.* J. Phys. Condens. Matter **23**, 305002 (2011).

47 Breckenfeld, E. *et al.* Effect of Growth Induced (Non)Stoichiometry on Interfacial Conductance in $LaAlO_3/SrTiO_3$. *Phys. Rev. Lett.* **110,** 196804 (2013).

48 Sato, H. K., Bell, C., Hikita, Y. & Hwang, H. Y. Stoichiometry control of the electronic properties of the $LaAlO_3/SrTiO_3$ heterointerface. *arXiv:1304.7830* (2013).

49 Cantoni, C. *et al.* Electron Transfer and Ionic Displacements at the Origin of the 2D Electron Gas at the LAO/STO Interface: Direct Measurements with Atomic-Column Spatial Resolution. *Advanced Materials* **24,** 3952-3957 (2012).

50 Liu, Z. Q. *et al.* Origin of the Two-Dimensional Electron Gas at $LaAlO_3/SrTiO_3$ Interfaces: The Role of Oxygen Vacancies and Electronic Reconstruction. *Phys. Rev. X* **3,** 021010 (2013).

51 Perdew, J. P., Burke, K. & Ernzerhof, M. Generalized gradient approximation made simple. *Phys. Rev. Lett.* **77,** 3865 – 3868 (1996).

52 Blöchl, P. E. Projector augmented-wave method. *Phys. Rev. B* **50,** 17953 – 17979 (1994).

53 Kresse, G. & Furthmüller, J. Efficient iterative schemes for ab initio total-energy calculations using a plane-wave basis set. *Phys. Rev. B* **54,** 11169 – 11186 (1996).

54 Kresse, G. & Joubert, D. From ultrasoft pseudopotentials to the projector augmented-wave method. *Phys. Rev. B* **59,** 1758 – 1775 (1999).

55 Kröger, F. A. & Vink, H. J. Relations between the concentrations of imperfections in crystalline solids. *Solid State Physics* **3,** 307 – 435 (1956).

56 Reuter, K. & Scheffler, M. Composition, structure, and stability of RuO_2 (110) as a function of oxygen pressure. *Phys. Rev. B* **65,** 035406 (2001).

57 Mitra, C., Lin, C., Robertson, J. & Demkov, A. A. Electronic structure of oxygen vacancies in $SrTiO_3$ and $LaAlO_3$. *Phys. Rev. B* **86,** 155105 (2012).